Published in final edited form as:
Magn Reson Med. 2013 January ; 69(1): 221–228. doi:10.1002/mrm.24232.

Blood Flow and Anatomical MRI in a Mouse Model of Retinitis Pigmentosa

Eric R Muir[1], **Bryan De La Garza**[1], and **Timothy Q Duong**[1,2,3,4,5,6]

[1]Research Imaging Institute, University of Texas Health Science Center, San Antonio, TX

[2]Department of Ophthalmology, University of Texas Health Science Center, San Antonio, TX

[3]Department of Radiology, University of Texas Health Science Center, San Antonio, TX

[4]Department of Physiology, University of Texas Health Science Center, San Antonio, TX

[5]South Texas Veterans Health Care System, San Antonio, TX

[6]Southwest National Primate Research Center, San Antonio, TX

Abstract

This study tested the sensitivity of an arterial spin labeling MRI method to image changes in retinal and choroidal blood flow (BF) and anatomical thickness of the retina in the rd10 mouse model of retinitis pigmentosa. High-resolution (42×42μm) MRI was performed on rd10 mice and age-matched controls at 25, 35, and 60 days of age (n=6 each group) on a 7-Tesla scanner. Anatomical MRI was acquired and quantitative BF was imaged using arterial spin labeling MRI with a separate cardiac labeling coil. Histology was obtained to confirm thickness changes in the retina. In control mice, the retinal and choroidal vascular layers were quantitatively resolved. In rd10 mice, retinal BF decreased progressively over time while choroidal BF was unchanged. The rd10 retina became progressively thinner at later time points compared to age-matched controls by anatomical MRI and histology ($p<0.01$). BF and anatomical MRI were capable of detecting decreased BF and thickness in the rd10 mouse retina. Because BF is tightly coupled to metabolic function, BF MRI has the potential to non-invasively assess retinal diseases in which metabolism and function are perturbed and to evaluate novel treatments, complementing existing retinal imaging techniques.

Keywords

retinal degeneration; retinitis pigmentosa; arterial spin labeling; blood flow; retina; choroid

INTRODUCTION

Retinitis pigmentosa (RP) is a group of inherited retinal diseases which cause retinal degeneration and vision loss, affecting 1.5 million people worldwide (1). It is characterized initially by a progressive loss of photoreceptors, with secondary deterioration of vascular and other cell layers (2). Most RP patients undergo a preliminary loss of peripheral vision and impaired night vision because rods are usually affected first. Secondary degeneration, usually including loss of cones, follows, resulting in the loss of central visual field, color vision, and potentially complete blindness (1). A large number of mutations in various genes

Correspondence: Timothy Duong, PhD, Research Imaging Center, UTHSCSA, 8403 Floyd Curl Dr, San Antonio, TX 78229, duongt@uthscsa.edu, Tel 210 567 8120, Fax 210 567 8152.

which cause RP have been described, including the genes for rhodopsin, mertk, and phosphodiesterase β(2- 4).

The rd10 mouse is an established animal model of RP (5-7). rd10 mice have a mutation in the *Pde6b* gene, encoding a subunit of the rod phosphodiesterase (5,6). Mutations in the gene for the β subunit of the rod phosphodiesterase have been found in human autosomal recessive RP (3). The mutation in the *Pde6b* gene causes deficient activity of the rod phosphodiesterase which results in the accumulation of cyclic GMP and death of rod cells (6). Based on histological data, retinal degeneration begins in rd10 mice about post natal 16 days and the outer nuclear layer and inner and outer segments completely degenerate by 60 days of age (6,7). Degeneration of the outer retina begins first with loss of rods, with cone loss and remodeling of the inner retina occurring later (7).

While the genetic aspects and thickness changes of RP are well studied, the lack of non-invasive, depth-resolved imaging techniques has limited the investigation of physiologic changes associated with retinal degeneration *in vivo*. Clinical examinations of RP include digital fundus photography using the 7 stereo fields (8), full-field electroretinography (ERG) (4), Goldmann visual field with V4e test object, and optical coherence tomography of the macula and optic disc and macular thickness (4). Many potential treatments (9), including vitamin A supplementation, intravitreal administration of growth factors (10), neuroprotective drugs (11), hyperoxia (12), gene therapy (13), and stem cell therapy (14), show potential to slow, halt, or reverse retinal degeneration. Non-invasive imaging technologies that can pinpoint layer-specific cellular and vascular changes may enable longitudinal staging of RP, objective measures of therapeutic interventions, and improved understanding of disease processes *in vivo*.

Vascular changes occur secondary to photoreceptor loss in RP (14-16), with atrophy of the retinal (14,15) and choroidal (17) vasculature. Histological studies showed leakage in the retinal vessels in Royal College of Surgeons (a model of RP) rats by 2 months of age (18). In a cat model of RP, retinal blood flow (rBF) was compromised while choroidal blood flow (chBF) was not significantly affected (19). In RP patients, diameter, blood velocity, blood flow (BF) in retinal veins, and total rBF were found to be lower (20), subfoveal chBF was lower (17), and chBF was reduced in late, but not early, stages of the disease (21). These findings suggest that there are vascular-specific (retinal and choroidal) changes accompanying retinal degenerations. Improved understanding of the physiological changes accompanying retinal degeneration may enable better understanding of the pathophysiology. BF changes may occur before irreversible degeneration, which could provide a potential objective measure of therapeutic interventions.

The goal of this study was to test whether anatomical and BF MRI techniques could detect changes of retinal thickness and possible changes of retinal and choroidal BF at different stages of retinal degeneration in the rd10 mouse model. Anatomical MRI was acquired using a balanced steady state free precession (bSSFP) sequence for fast image acquisition with high signal-to-noise ratio. BF MRI used cardiac spin labeling (CSL) MRI (22) which is based on the continuous arterial spin labeling technique with a separate cardiac coil to avoid saturation of the imaging signal in the retina due to the small size of mice.

METHODS

Animal preparation

Experiments were performed on rd10 mice which are homozygous for the Pde6b mutation and bred onto a C57BL/6J background (Jackson Laboratory, Bar Harbor, Maine). For controls, normal age-matched C57BL/6J mice were used (Jackson Laboratory, Bar Harbor,

Maine). MRI and histology were performed on mice at post-natal ages 25, 35, and 60 days (P25, P35, and P60, n=6 control and 6 rd10 per age group). The exact ages for the three groups ranged from 23-26 days, 35-37 days, and 59-60 days. Imaging earlier time points than P25 was not done because of difficulty in monitoring physiology in smaller mice.

Animals were placed into a head holder with ear and tooth bars, and breathed spontaneously under 1.0-1.1% isoflurane, 30% O_2 with balance N_2. Rectal temperature was maintained at 37±0.5°C via a circulating warm water pad. Respiration rate, heart rate, and oxygen saturation were continuously monitored (MouseOx, STARR Life Science Corp., Oakmont, PA).

MRI

MRI studies were performed on a 7Tesla, 30-cm bore magnet and a 150G/cm BGA6S gradient insert (Bruker, Billerica, MA), which had a 6-cm clear bore. BF MRI used the cardiac labeling technique (23). For imaging, a small circular surface eye coil with active decoupling (0.6cm diameter) was placed over the left eye. A circular labeling coil (0.8cm diameter) was placed at the heart position for cardiac spin labeling (23).

BF MRI was acquired using two-coil continuous arterial spin labeling (ASL) with an echo planar imaging (EPI) sequence. Paired images, one with and one without labeling, were acquired in an interleaved fashion. The axial labeling plane was positioned at the heart position and the label duration was 2.6s, as described previously (23). Images were acquired in a coronal orientation with a single slice through the optic nerve head, angled perpendicular to the retina. Two-segment, gradient-echo EPI was used with field of view=6×6mm, matrix=144×144 (42×42μm resolution), post-labeling delay=350ms, a single 0.4mm slice, TR=3s per segment, and TE=9.7ms in 25 and 60 day old mice or 12.6ms for 35 day old mice. For each scan, 100 pairs of images were acquired in time-series, totaling 20min.

Anatomical images were acquired using a bSSFP sequence with a field of view=5×5mm, matrix=120×120 (42×42μm), a single 0.4mm slice, and TE/TR=3.6/7.2ms. Data were oversampled by a factor of two in both the frequency and phase-encode directions. Fifty repetitions were acquired in time-series with 3 averages per repetition, totaling 4.5min.

Data analysis

Image analysis was done using codes written in Matlab (Math-Works, Natick, MA), STIMULATE software (University of Minnesota), and Statistical Parametric Mapping 5 (SPM5). Images for BF calculation were zero-padded to 256×256 (nominal resolution of 23×23μm) before Fourier transform into imaging space. Anatomical images were zero-padded to 128×128 (nominal resolution of 39×39μm). Images were acquired in time series, aligned using the spatial realignment function in SPM5 and averaged off line.

BF images of the eye, S_{BF}, in units of (ml blood)/(g tissue)/min were calculated pixel-by-pixel using $S_{BF}=\lambda/T_1[(S_{NL}-S_L)/(S_L+(2\alpha-1)S_{NL})]$, (24) where S_{NL} and S_L are signal intensities of the non-labeled and labeled images, respectively.λ, the water tissue-blood partition coefficient, was taken to be 0.9, the same as the brain (25).λ has not been reported for the retina or choroid. The whole-retina T_1 value at 7T ranged from 1.6-1.9s and 1.8s was used for both retina and choroid T_1, which is also similar to brain T_1 at 7T (26). MRI BF is inversely proportional to T_1 and thus such T_1 error would scale accordingly. The labeling efficiency α was previously measured to be 0.7 in the distal internal carotid arteries at the base of the frontal lobe (23).

Quantitative analysis of anatomical thickness and BF values were performed (22,27). Anatomical and BF intensity profiles across the retinal thickness were obtained by projecting lines perpendicular to the inner edge of the retina with profiles obtained at 4x spatial interpolation (22,27). Further motion correction was performed on the extracted profiles in Matlab (28). BF profiles were averaged along the length of the retina, excluding the region around the optic nerve head. Anatomical profiles were averaged over two 273μm long regions located on either side of the optic nerve head. Measurements of BF peak values and layer thicknesses – defined as the half-height width of the anatomical peaks – were determined from the average profiles for each animal. In animals in which the rBF layer could not be clearly distinguished, as was common in the rd10 mice at P35 and P60, the location at which to measure rBF was determined from the EPI anatomical profile.

Statistical analysis was performed using SPSS and Matlab. rBF, chBF, and histological thicknesses were analyzed using two-way ANOVA. Levene's test was used to assess equality of variances. For data with equal variances ($p>0.05$, chBF and inner and outer retinal thickness from histology), multiple comparisons were made using the Tukey-Kramer method. For data with unequal variances ($p<0.05$, rBF and total neural retinal thickness from histology), multiple comparisons were made using Dunnett's T3. Thickness measurements from MRI were made on the data interpolated to 5.9μm producing a discrete and non-normal distribution. As such, thickness measurements from MRI were compared using the non-parametric Wilcoxon rank-sum test. MRI and histological thickness were compared using the Wilcoxon rank-sum test. For all statistical tests, $p<0.05$ was considered significant.

Histology

For histology, the mice were euthanized and the left eyes were enucleated and placed in 10% neutral buffered formalin overnight. Eyes were then dehydrated with washes of ethanol and xylene. Eyes were embedded in paraffin and sectioned at 8μm on a microtome. Multiple slices through the optic nerve were obtained and stained using hematoxylin and eosin. Thickness measurements were made at 100x with an Olympus BX60 microscope and averaged from 2 different slices with measurements made ±250μm away from the optic nerve head, on both sides. Histology and MRI were performed on the same animals in the P25 and P60 age groups and on separate animals in the P35 group.

RESULTS

Table 1 shows the physiological parameters – weight, respiration rate, heart rate, and arterial oxygen saturation – of the control and rd10 mice during acquisition of BF MRI. Weight was 2 grams less in P25 rd10 mice compared to age-matched controls ($p<0.01$). The remaining physiological parameters were not statistically different between aged-matched control and rd10 mice ($p>0.05$, two-sided unpaired t-tests).

Histology demonstrated substantial degeneration of the rd10 retina at P25, P35, and P60 (Figure 1). In P60 rd10 mice the inner/outer segments could no longer be detected. The outer nuclear/outer plexiform layers could not be distinguished from each other, so a single value was given for both layers. In P25 and P35 rd10 mice the inner/outer segments could not be distinguished from each other, so a single value was reported for both layers. Anatomical layer thicknesses are summarized in Table 2. Two-way ANOVA was separately run on the total neural retina, outer retina (OPL, ONL, IS, and OS), and inner retina (GCL, IPL, and INL). In P60 rd10 mice, both the inner and outer retina were significantly thinner compared to P25 and P35 rd10 mice ($p<0.05$) and controls at all ages ($p<0.001$). The outer retina of P60 rd10 mice was also thinner than that of P35 rd10 mice ($p<0.05$). In P35 rd10 mice, the inner retina was only significantly thinner compared to P25 controls ($p<0.01$), and the outer retina was thinner than P25 rd10 mice ($p<0.05$) and all control mice ($p<0.001$). In P25 rd10

mice, the outer layers of the retina were significantly thinner ($p<0.001$) while the inner retina was unchanged ($p>0.05$) compared to controls at all ages. There were no significant thickness differences between any ages of the control mice ($p>0.05$).

Representative MRI anatomical images (42×42×400μm) and group-average profiles of normal and rd10 mice at P25, P35, and P60 are shown in Figure 2. In the control mice, 4 layers were present in the retina (including a layer that was the choroid) at all ages. In rd10 mice at all ages, there were only 2 MRI layers in the retina (including the choroid). Thicknesses of histological and MRI anatomical layers are summarized in Figure 3. Neural retinal thickness was normalized to the average thickness of P60 control mice (231 and 182μm from histology and MRI, respectively). The average total thickness from MRI of the retina and choroid in control mice was 239μm. The thickness of the neural retina was significantly less in rd10 mice compared to age-matched controls at P25, P35 and P60, but the thickness of the choroid (MRI layer 4) was not changed. In rd10 mice, the neural retina was significantly thinner at P35 and P60 compared to P25 rd10 mice ($p<0.01$). MRI neural retinal thickness was significantly less compared to histological thickness in each group of animals ($p<0.01$).

BF images from control and rd10 mice are shown in Figure 4. Group-averaged BF profiles from control and rd10 mice at P25, P35 and P60 are shown in Figure 5. In the control mice at all ages, two BF peaks, corresponding to rBF and chBF, were present and were separated by a region with low BF that corresponded to the avascular region (outer nuclear layer and inner/outer segments). In rd10 mice, the chBF peak was easily distinguished at all ages, but the rBF peak was not as clear. At P25 there was an obvious rBF layer, but it was not well separated from chBF. At P35 days, there was a weak layer in the BF images that was likely the rBF, but it was not separated from chBF and was generally difficult to distinguish from noise. At P60, rBF was even more difficult to detect, and could not generally be distinguished. The anatomical profiles from the EPI images are also shown in Figure 5, demonstrating the correspondence of BF to the EPI anatomy which was used to determine the location of rBF in most rd10 mice.

Values of rBF and chBF are summarized in Figure 6. The results of ANOVA showed a significant effect on rBF ($p<0.01$) and chBF ($p<0.05$) between rd10 and control mice. Age did not have a significant effect on rBF or chBF ($p>0.05$). Comparisons of groups showed that rBF of P60 rd10 mice was significantly less than P25 and P60 controls as well as P25 rd10 mice. In P35 rd10 mice, rBF was significantly lower compared to P60 controls. Additionally, chBF in P25 controls was significantly less than P35 rd10 mice.

DISCUSSION

Novel non-invasive, high-resolution MRI approaches were applied to image perturbations of anatomical thickness and quantitative BF in the mouse retina with laminar resolution in a model of RP. MRI BF measures tissue perfusion in quantitative units of ml/g/min, in contrast to blood velocity and diameter measurements often reported in optical imaging literature. MRI detects progressive anatomical and BF changes at different stages of disease in the retina of the rd10 mouse model of RP. rBF is reduced but chBF is unchanged. While MRI has low spatiotemporal resolution compared to optics, the unique advantage of MRI is that it offers physiological data with a large field of view and is not depth limited. Because BF is tightly coupled to metabolic function, it may provide a non-invasive measure of tissue pathophysiology in which basal metabolism and function are perturbed.

MRI contrasts and layers

There were four dark-bright-dark-bright anatomical layers in the mouse retina and choroid in bSSFP images, as described previously (28), and consistent with T_2-weighted and diffusion-weighted MRI of the mouse eye at 47×47×400μm (29-31). These studies concluded that the outermost of the 3 retinal layers was the photoreceptor cells (outer nuclear layer and inner/outer segments), and that the two inner layers of the retina were the inner nuclear/outer plexiform layers and the nerve fiber/ganglion cell/inner plexiform layers based on the directionality of water diffusion (30,31) or blood level oxygenation dependent (BOLD) changes to hypoxia (28). The 3 retinal layers found with bSSFP in the control mice likely correspond to these same layers (28). In the rd1 mouse model of RP at 2-4 months of age, T_2-weighted and diffusion-weighted MRI also revealed two layers in the retina, including the choroid (30,31), consistent with our bSSFP data in the rd10 mice. The remaining MRI layer of the neural retina rd1 mice was thought to be the nerve fiber/ganglion cell/inner plexiform layers, while the inner nuclear/outer plexiform layers were believed to be indistinguishable from the choroid (30,31). Changes in thickness were not reported in these previous studies. Degeneration in the rd10 and rd1 mouse is similar, but the rd1 degeneration has early onset and is more rapid, so MRI detection of retinal thinning over time is likely difficult compared to the slower degenerating rd10 retina (6).

Three bright-dark-bright anatomical layers have been found in the rat retina and choroid using T_1-weighted gradient-echo MRI at 60×60×500μm (27). The outer bright layer was believed to be the choroid, the middle dark layer the avascular photoreceptor cells (outer nuclear layer and inner/outer segments), and the inner bright layer the nerve fiber/ganglion cell/inner plexiform/inner nuclear layers (27). The inner and outer bright layers were enhanced by intravascular gadolinium, corresponding to the retinal and choroidal vessels (27,32). In the Royal College of Surgeons rat model of RP at P120, only a single bright layer was detected (27), likely corresponding to the choroid combined with the bright inner layer (nerve fiber/ganglion cell/inner plexiform/inner nuclear layers). Gadolinium enhanced the entire remaining layer demonstrating the loss of the avascular outer layers of the retina. Of note manganese-enhanced MRI has been used as a of measure ionic regulation to detect early changes in animal models of RP (33).

Retinal thickness and anatomical MRI

The neural retina was substantially thinner in the rd10 mice compared to age-matched controls. The thickness of the choroid did not change, as expected. The rate of retinal degeneration varied across time. The photoreceptors in rd10 mice degenerated rapidly between 16 to 30 days of age, during which time most of the retinal degeneration occurs (6,7). This is consistent with the large histological changes between P25 and P35 mice but slight change between P35 and P60 found herein. In rd10 mice, the inner retinal layers undergo extensive remodeling (34), and about 20% of bipolar cells (in the inner nuclear layer) are lost between 1.5 and 3.5 months (7). The inner nuclear layer is thinner in rd10 mice by 6 months of age (35), and the inner retina is slightly thinned in rd1 mice (36).

At 42×42×400μm resolution, MRI could non-invasively detect differences in retinal thickness between age-matched rd10 mice and controls at all ages and thinning of the rd10 retina over time, with the retina being substantially thinner at P35 and P60 compared to P25. Both MRI and histology detected thinning of the retina, but the thicknesses from MRI were less than those from histology. However, the difference in thickness between age-matched control and rd10 mice was similar from MRI (67, 107, and 117μm at P25, P35, and P60, respectively) and histology (92, 104, and 133μm at P25, P35, and P60 respectively).

Possible reasons for the discrepancy include distortion of the tissue during fixation and processing for histology and partial volume effect in MRI. We have found that fixation using pre-mixed formalin (used herein) was different from using fresh-made paraformaldehyde, with pre-mixed formalin yielding thicker retinas compared to fresh-made fixative (data not shown). Partial volume and the relatively low spatial resolution of MRI will limit the precision and accuracy of MRI derived thicknesses. Neural retinal thickness in mice from MRI at 47×47μm, frozen histology, and paraformaldehyde-fixed histology were 182, 220, and 159μm, respectively (29). With MRI at 23×23μm, retinal thickness in mice was 207-224μm (37). Thickness in rats from MRI at 60×60μm and paraformaldehyde-fixed histology were 180 and 169um, respectively (27). Interestingly, the MRI thickness measurements appear to be more consistent than histology despite the limited MRI resolution, suggesting histological preparation can substantially effect retinal fixation. However, limited MRI spatial resolution will greatly limit precision of retinal thickness measurements.

BF measurement

In normal controls, two separated BF layers, corresponding to rBF and chBF, could be distinguished. In P25 rd10 mice, the rBF and chBF layers were clearly present in all mice, but were not separated well. In rd10 mice at P35 and P60, the chBF layer was still obvious, but rBF was difficult to detect, particularly at P60. The difficulty in detecting the rBF layer at later stages of retinal degeneration could be due to reduced rBF or insufficient spatial resolution to detect the vascular layer of the thinned retina. The thinning of the avascular outer retina results in the vascularized inner retina and the choroid moving closer together. Based on the anatomical profiles of the EPI images, however, the neural retina was thick enough to be distinguished, and thus, rBF should still be able to be detected by MRI in principle.

Partial volume effect from the choroid would be expected to cause overestimation of rBF. However, rBF was consistently reduced in rd10 mice, suggesting that partial volume effect from chBF did not completely overwhelm the rBF. Nonetheless, partial volume effect from the choroid could confound interpretation. In the worst case, there may be essentially no rBF in rd10 mice at P35 and P60 and the measured rBF was just the tail of the chBF peak. Future studies at higher resolution are needed to better model the data and to elucidate contribution of partial volume effect. Partial volume effects and atrophy artifacts could also lead to underestimated rBF. For instance, increased partial volume from the vitreous would cause underestimation of rBF, although since the vascularized inner retina had only slight thinning, we expect increased partial volume effect from the vitreous would be less compared to increased partial volume from the choroid.

In normal conditions, the retinal vessels are embedded in the inner retina and the outer retina is avascular. Another factor to consider is whether labeled vascular water could exchange into tissue and diffuse into or across the avascular region. In controls, the two BF peaks from the choroid and the inner retina were separated by a BF minimum, suggesting there may be little diffusion of spin-labeled water from one vascular layer to the other but this remains to be investigated. In controls, the thickness of the avascular layer (>100μm) and the inner and outer blood retina barriers would limit diffusion from one vasculature to the other. In rd mice, however, blood retina barrier permeability increases (31) and the avascular region almost completely degenerates, so some labeled water from the choroid may perfuse into the remaining retina, contributing to the low rBF signal. Measurement of permeability changes specific to the retinal pigment epithelium (the outer blood retina barrier) would be difficult and were not accounted for in this study. A possible way to further investigate this would be to ablate the retinal vessels or to use animals which lack retinal vessels, such as such the guinea pig or rabbit (38).

In the rd10 mouse model of RP, rBF showed progressive reduction with age, but was only significantly reduced at P60. ChBF was unaffected in rd10 mice up to P60, although it remains possible that the chBF could be affected in older mice. In P25 controls, chBF was significantly lower compared to P35 rd10 mice, but chBF was otherwise consistent among all groups. Due to the lack of any other differences in chBF this may be an error due to the small sample sizes per group. Previous studies of RP also reported reduced rBF and potentially reduced chBF. In a cat model of RP, rBF was compromised while chBF was not significantly affected (19). In humans, diameter, blood velocity, and BF in retinal veins were all lower in RP patients, as well as total rBF (20). In another study of human RP, the ocular pulse amplitude, an indication of chBF, was found to be reduced in late, but not early, stages of the disease (21). In yet another study using laser Doppler flowmetry, chBF was reduced in human RP (17). In rd1 mice loss of the choriocapillaris does occur, but not until 10 weeks of age (39). By 16 months of age, only 5-10% of the choriocapillaris is atrophied (39), so it is not surprising that chBF was not reduced in rd10 mice at only P60. Possible explanations for the apparent discrepancies among different studies could be due to differences between animal models and human RP, stages of disease, and/or measurement methods. It is also possible that there are regional reductions in chBF.

The causes of reduced rBF could be multifactorial. There is evidence that attenuation of retinal vasculature in RP is due to hyperoxia in the retina, caused by the loss of the metabolically active photoreceptors (16,40-42). Royal College of Surgeons rats have higher tissue oxygen levels in the retina, increased delivery of oxygen from the choroid to the inner retina, and reduced oxygen input from the retinal circulation (41,43). In Abyssinian cats, inner retinal oxygen is unaltered while the retinal vessels attenuate, possibly to maintain normal tissue oxygenation (42). Another possibility is that reduced rBF is a result of reduced metabolic needs of the inner retina due to decreased signaling from the degenerating photoreceptors. The retinal vasculature regulates BF in response to the oxygen levels and metabolic needs of the inner retina (40). However, the choroid has little or no response to oxygenation or metabolic needs of the retina (40), a possible reason for the unchanged chBF in the rd10 mice. Additionally, the inner retina undergoes extensive remodeling, which could alter its function and metabolism or possibly directly affect vascular structure (44).

CONCLUSIONS

This study demonstrates that MRI methods could detect anatomical and blood flow changes in the rd10 mouse model of retinitis pigmentosa with layer specificity, depth resolution, and a large field of view. Future studies will investigate evoked responses and vascular reactivity as potential imaging markers for early detection and longitudinal monitoring of therapeutic treatments in retinal degeneration as well as other retinal diseases, such as diabetic retinopathy. MRI has the potential to provide clinically relevant physiological and functional data non-invasively, complementing existing imaging techniques.

Acknowledgments

Grant support: This work was supported in part by the NIH/NEI (R01 EY014211, EY018855, and R01EY09702), and a MERIT Award from the Department of Veterans Affairs, and a Clinical Translational Science Award Supplement (parent grant UL1RR025767). ERM was supported in part by NIH 5T32HL007446-29.

References

1. Berson EL. Retinitis pigmentosa. The Friedenwald lecture. Invest Ophthalmo Vis Sci. 1993; 34:1659–1676.
2. Jones BW, Watt CB, Marc RE. Retinal remodeling. Clin Exp Optom. 2005; 88:282–291. [PubMed: 16255687]

3. McLaughlin ME, Sandberg MA, Berson EL, Dryja TP. Recessive mutations in the gene encoding the beta-subunit of rod phosphodiesterase in patients with retinitis pigmentosa. Nature Genetics. 1993; 4:130–134. [PubMed: 8394174]
4. Bessant, DAR.; Kaushal, S.; Bhattacharya, SS. Genetics and Biology of the Inherited Retinal Dystrophies. In: Alm, A.; Ehinger, BEJ.; Kaufman, PL., editors. Adler's Physiology of the Eye. 10. St. Louis: Mosby; 2003. p. 358-377.
5. Chang B, Hawes NL, Hurd RE, Davisson MT, Nusinowitz S, Heckenlively JR. Retinal degeneration mutants in the mouse. Vision Research. 2002; 42:517–525. [PubMed: 11853768]
6. Chang B, Hawes NL, Pardue MT, German AM, Hurd RE, Davisson MT, Nusinowitz S, Rengarajan K, Boyd AP, Sidney SS, Phillips MJ, Stewart RE, Chaudhury R, Nickerson JM, Heckenlively JR, Boatright JH. Two Mouse Retinal Degenerations Daused by Missense Mutations in the beta-subunit of Rod cGMP Phosphodiesterase Gene. Vision Research. 2007; 47:624–633. [PubMed: 17267005]
7. Gargini C, Terzibasi E, Mazzoni F, Strettoi E. Retinal Organization in the Retinal Degeneration 10 (rd10) Mutant Mouse: A Morphological and ERG Study. J Comp Neurol. 2007; 500:222–238. [PubMed: 17111372]
8. Photocoagulation for diabetic macular edema. Early Treatment Diabetic Retinopathy Study report number 1. Early Treatment Diabetic Retinopathy Study research group. Arch Ophthalmol. 1985; 103:1796–1806. [PubMed: 2866759]
9. Kalloniatis M, Fletcher EL. Retinitis pigmentosa: understanding the clinical presentation, mechanisms and treatment options. Clin Exp Optom. 2004; 87:65–80. [PubMed: 15040773]
10. Sieving PA, Caruso RC, Tao W, Coleman HR, Thompson DJ, Fullmer KR, Bush RA. Ciliary neurotrophic factor (CNTF) for human retinal degeneration: phase I trial of CNTF delivered by encapsulated cell intraocular implants. Proc Natl Acad Sci USA. 2006; 103:3896–1901. [PubMed: 16505355]
11. Chao HM, Chidlow G, Melena J, Wood JP, Osborne NN. An investigation into the potential mechanisms underlying the neuroprotective effect of clonidine in the retina. Brain Res. 2000; 877:47–57. [PubMed: 10980242]
12. Vingolo EM, Rocco M, Grenga PL, Salvatore S, Pelaia P. Slowing the degenerative process, long lasting effect of hyperbaric oxygen therapy in retinitis pigmentosa. Graefes Arch Clin Exp Ophthalmol. 2008; 246:93–98. [PubMed: 17674017]
13. Acland GM, Aguirre GD, Ray J, Zhang Q, Aleman TS, Cideciyan AV, Pearce-Kelling SE, Anand V, Zeng Y, Magure AM, Jacobson SG, Hauswirth WW, Bennett J. Gene therapy restores vision in a canine model of childhood blindness. Nat Genet. 2001; 28:92–95. [PubMed: 11326284]
14. Otani A, Dorrell MI, Kinder K, Moreno SK, Nusinowitz S, Banin E, Heckenlively J, Friedlander M. Rescue of retinal degeneration by intravitreally injected adult bone marrow-derived lineage-negative hematopoietic stem cells. J Clin Invest. 2004; 114:765–774. [PubMed: 15372100]
15. Pennesi ME, Nishikawa S, Matthes MT, Yasumura D, LaVail MM. The relationship of photoreceptor degeneration to retinal vascular development and loss in mutant rhodopsin transgenic and RCS rats. Exp Eye Res. 2008; 87:561–570. [PubMed: 18848932]
16. Penn JS, Li S, Naash MI. Ambient hypoxia reverses retinal vascular attenuation in a transgenic mouse model of autosomal dominant retinitis pigmentosa. Invest Ophthalmol Vis Sci. 2000; 41:4007–4013. [PubMed: 11053306]
17. Falsini B, Anselmi GM, Marangoni D, D'Esposito F, Fadda A, Renzo AD, Campos EC, Riva CE. Subfoveal choroidal blood flow and central retinal function in retinitis pigmentosa. Invest Ophthalmol Vis Sci. 2011; 52:1064–1069. [PubMed: 20861481]
18. Wang S, Villegas-Perez MP, Holmes T, Lawrence MM, Vidal-Sanz M, Hurtado-Montalban N, Lund RD. Evolving neurovascular relationships in the RCS rat with age. Current Eye Res. 2003; 27:183–196.
19. Nilsson SFE, Maepea O, Alm A, Narfstrom K. Ocular blood flow and retinal metabolism in Abyssinina cats with hereditary retinal degeneration. Invest Ophthalmol Vis Sci. 2001; 42:1038–1044. [PubMed: 11274083]
20. Grunwald JE, Maguire AM, DuPont J. Retinal hemodynamics in retinitis pigmentosa. Am J Ophthalmol. 1996; 122:502–508. [PubMed: 8862046]

21. Schmidt K-G, Pillunat LE, Kohler K, Flammer J. Ocular pulse amplitude is reduced in patients with advanced retinitis pigmentosa. Br J Ophthalmol. 2001; 85:678–682. [PubMed: 11371487]
22. Muir ER, Duong TQ. MRI of retinal and choroidal blood flow with laminar resolution. NMR Biomed. 2011; 24:216–223. [PubMed: 20821409]
23. Muir ER, Shen Q, Duong TQ. Cerebral blood flow MRI in mice using the cardiac spin-labeling technique. Magn Reson Med. 2008; 60:744–748. [PubMed: 18727091]
24. Shen Q, Ren H, Cheng H, Fisher M, Duong TQ. Functional, perfusion and diffusion MRI of acute focal ischemic brain injury. J Cereb Blood Flow and Metab. 2005; 25:1265–1279. [PubMed: 15858531]
25. Herscovitch P, Raichle ME. What is the correct value for the brain-blood partition coefficient for water? J Cereb Blood Flow Metab. 1985; 5:65–69. [PubMed: 3871783]
26. Nair G, Shen Q, Duong TQ. Relaxation time constants and apparent diffusion coefficients of rat retina at 7 Tesla. Int J Imaging Syst Technol. 2010; 20:126–130.
27. Cheng H, Nair G, Walker TA, Kim MK, Pardue MT, Thule PM, Olson DE, Duong TQ. Structural and functional MRI reveals multiple retinal layers. Proc Natl Acad Sci USA. 2006; 103:17525–17530. [PubMed: 17088544]
28. Muir ER, Duong TQ. Layer-specific functional and anatomical MRI of the retina with passband balanced SSFP. Magn Reson Med. 2011; 66:1416–1421. [PubMed: 21604296]
29. Chen J, Wang Q, Zhang J, Yang X, Wang J, Berkowitz BA, Wickline SA, Song SK. In vivo quantification of T1, T2, and apparent diffusion coefficient in the mouse retina at 11.74T. Magn Reson Med. 2008; 59:731–738. [PubMed: 18383302]
30. Chen J, Wang Q, Chen S, Wickline SA, Song SK. In vivo diffusion tensor MRI of the mouse retina: a noninvasive visualization of tissue organization. NMR Biomed. 2011; 24:447–451. [PubMed: 20931570]
31. Wang Q, Song SK, Zhang H, Berkowitz BA, Chen S, Wickline SA, Chen J. Photoreceptor degeneration changes magnetic resonance imaging features in a mouse model of retinitis pigmentosa. Magn Reson Med. 2011; 65:1793–1798. [PubMed: 21590807]
32. Shen Q, Cheng H, Chang TF, Nair G, Shonat RD, Pardue MT, Toi VV, Duong TQ. Magnetic resonance imaging of anatomical and vascular layers of the cat retina. J Magn Reson Imaging. 2006; 23:465–472. [PubMed: 16523482]
33. Berkowitz BA, Gradianu M, Schafer S, Jin Y, Porchia A, Iezzi R, Roberts R. Ionic dysregulatory phenotyping of pathologic retinal thinning with manganese-enhanced MRI. Invest Ophthalmol Vis Sci. 2008; 49:3178–3184. [PubMed: 18362105]
34. Barhoum R, Martinez-Navarrete G, Corrochano S, Germain F, Fernandez-Sanchez L, de la Rosa EJ, de la Villa P, Cuenca N. Functional and structural modifications during retinal degeneration in the rd10 mouse. Neuroscience. 2008; 155:698–713. [PubMed: 18639614]
35. Pang JJ, Dai X, Boye SE, Barone I, Boye SL, Mao S, Everhart D, Dinculescu A, Liu L, Umino Y, Lei B, Chang B, Barlow R, Strettoi E, Hauswirth WW. Long-term retinal function and structure rescue using capsid mutant AAV8 vector in the rd10 mouse, a model of recessive retinitis pigmentosa. Mol Ther. 2011; 19:234–242. [PubMed: 21139570]
36. Huber G, Beck SC, Grimm C, Sahaboglu-Tekgoz A, Paquet-Durand F, Wenzel A, Humphries P, Redmond TM, Seeliger MW, Fischer MD. Spectral domain optical coherence tomography in mouse models of retinal degeneration. Invest Ophthalmol Vis Sci. 2009; 50:5888–5895. [PubMed: 19661229]
37. Calkins DJ, Horner PJ, Roberts R, Gradianu M, Berkowitz BA. Manganese-enhanced MRI of the DBA/2J mouse model of hereditary glaucoma. Invest Ophthalmol Vis Sci. 2008; 49:5083–5088. [PubMed: 18552381]
38. Sen HA, Berkowitz BA, Ando N, de Juan E Jr. In vivo imaging of breakdown of the inner and outer blood-retinal barriers. Invest Ophthalmol Vis Sci. 1992; 33:3507–3512. [PubMed: 1464497]
39. Neuhardt T, May CA, Wilsch C, Eichhorn M, Lutjen-Drecoll E. Morphological changes of retinal pigment epithelium and choroid in rd-mice. Exp Eye Res. 1999; 68:75–83. [PubMed: 9986744]
40. Stone, J.; Valter, K. Roles of Oxygen in the Stability of Photoreceptors. In: Chalupa, LM.; Williams, RW., editors. Eye, Retina, and Visual System of the Mouse. Cambridge: MIT Press; 2008. p. 559-572.

41. Yu DY, Cringle SJ. Retinal degeneration and local oxygen metabolism. Exp Eye Res. 2005; 80:745–751. [PubMed: 15939030]
42. Padnick-Silver L, Kang Derwent JJ, Giuliano E, Narfstrom K, Linsenmeier RA. Retinal oxygenation and oxygen metabolism in Abyssinian cats with a hereditary retinal degeneration. Invest Ophthalmol Vis Sci. 2006; 47:3683–3689. [PubMed: 16877443]
43. Yu DY, Cringle S, Valter K, Walsh N, Lee D, Stone J. Photoreceptor death, trophic factor expression, retinal oxygen status, and photoreceptor function in the P23H rat. Invest Ophthalmol Vis Sci. 2004; 2004:2013–2019. [PubMed: 15161870]
44. Jones BW, Watt CB, Marc RE. Retinal remodelling. Clin Exp Optom. 2005; 88:282–291. [PubMed: 16255687]

Abbreviations

BF	blood flow
chBF	choroidal blood flow
rBF	retinal blood flow
ASL	arterial spin labeling
CSL	cardiac spin labeling
EPI	echo planar imaging
SD	standard deviation
RP	retinitis pigmentosa
ERG	electroretinogram

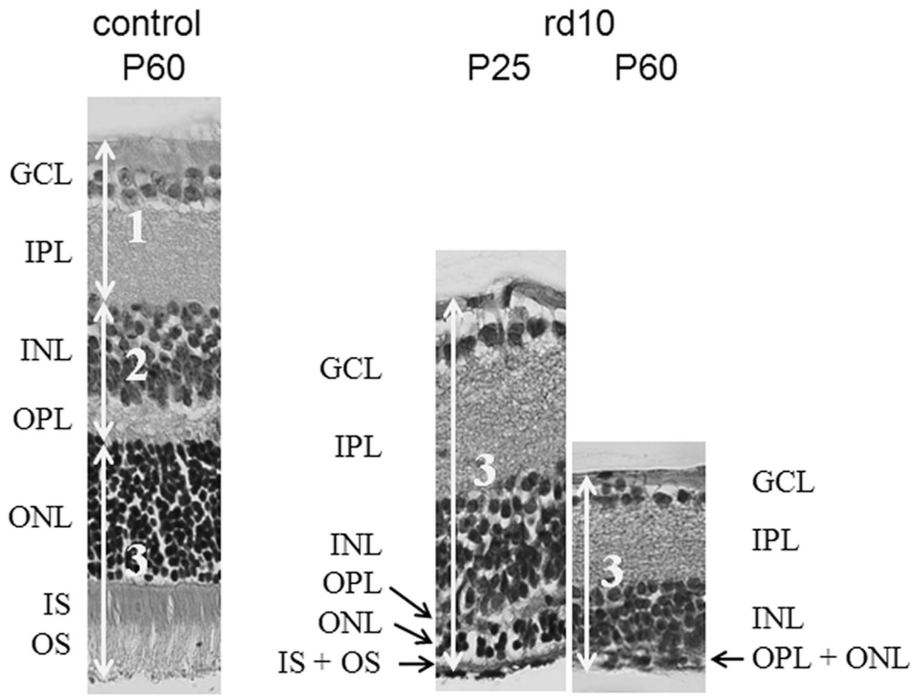

Figure 1.
Histology from control and rd10 mouse retinas obtained at 40x magnification. The numbered arrows correspond to the proposed anatomical MRI layers (see Figure 2). GCL – ganglion cell and nerve fiber layers, IPL – inner plexiform layer, INL – inner nuclear layer, OPL – outer plexiform layer, ONL – outer nuclear layer, IS – inner segment, OS – outer segment.

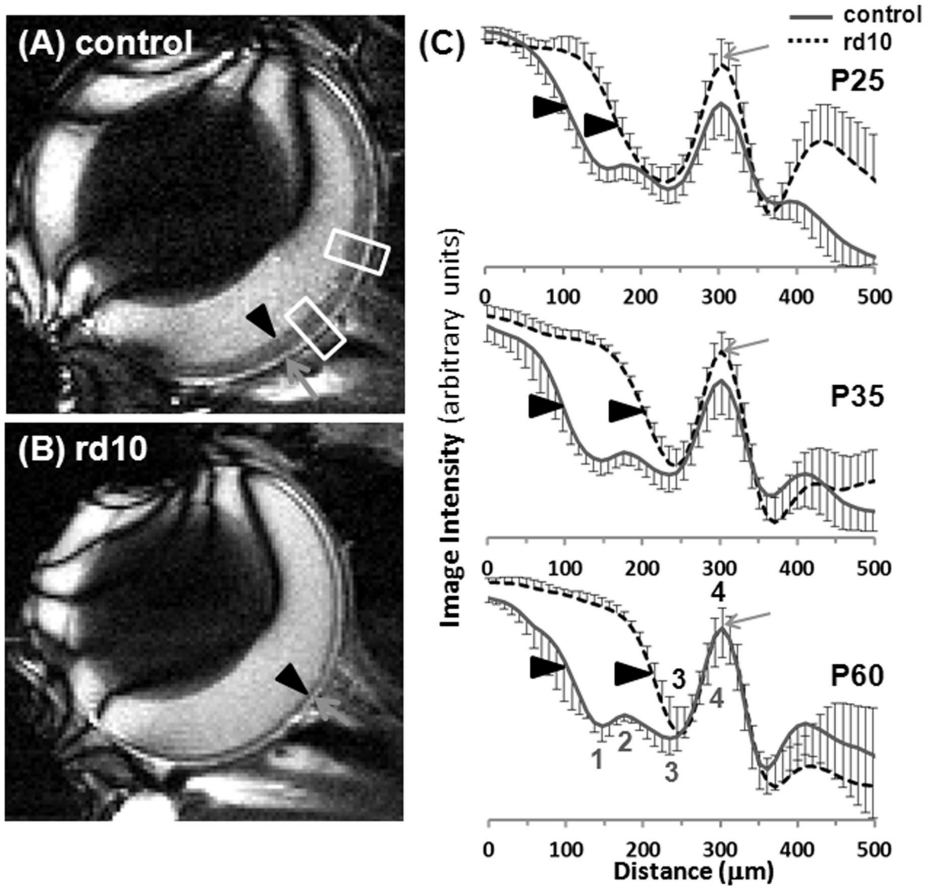

Figure 2.

Anatomical images at 42×42×400μm from a single (A) control and (B) rd10 mouse at P60. (C) The group average anatomical profiles for control mice at P25, P35, and P60 (n=6 at each age) and for rd10 mice at P25, P35, and P60 (n=6 at each age). The choroid peaks from all profiles were aligned together. Four layers were present in the control retina, including the choroid (labeled 1-4 in red below the profiles). Two layers were present in the rd10 retina, including the choroid (labeled 3-4 in blue above the profiles). Layer 3 likely corresponds to different anatomical layers in the control and rd10 retina. Error bars are SD. The green arrows indicate the choroid (layer 4). The black arrowheads indicate the vitreous-retina edge. The white boxes indicate the two 273μm wide regions from where the profiles were obtained. To avoid blurring in the group average profiles a 1D spatial transformation, including translation and scaling, was performed so that the 4 (or 2) labeled maxima and minima from each animal were aligned to all other animals in the group. Profiles were normalized by their maximum and minimum values before calculation of mean and SD.

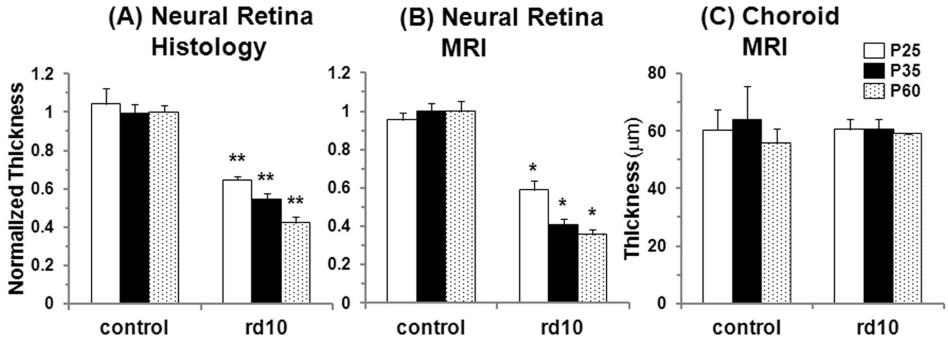

Figure 3.

Group-averaged normalized thicknesses of the neural retina from (A) histology and (B) anatomical MRI (sum of MRI layers 1, 2, and 3) at 42×42×400μm from control and rd10 mice at P25, P35, and P60. (C) Group-averaged absolute thicknesses of the choroid from anatomical MRI (MRI layer 4). Error bars represent SD. *p<0.01 compared to age-matched control mice, **p<1E-6 compared to age-matched control mice. From MRI, P35 and P60 rd10 mice also had significantly thinner retinas compared to P25 rd10 mice, p<0.01. From histology, P60 rd10 mice had significantly thinner retinas compared to P25 and P35 rd10 mice, p<0.01, and P35 rd10 mice had thinner retinas compared to P25 rd10 mice, p<0.05.

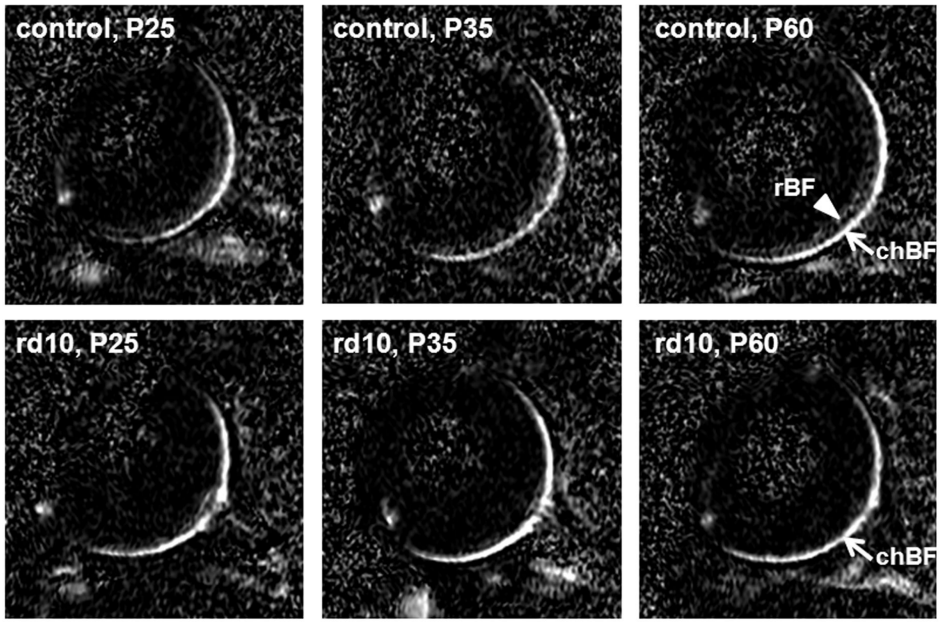

Figure 4.
Blood flow images at 42×42×400μm from control and rd10 mice at P25, P35, and P60. The arrows indicate chBF and the white arrowhead indicates rBF.

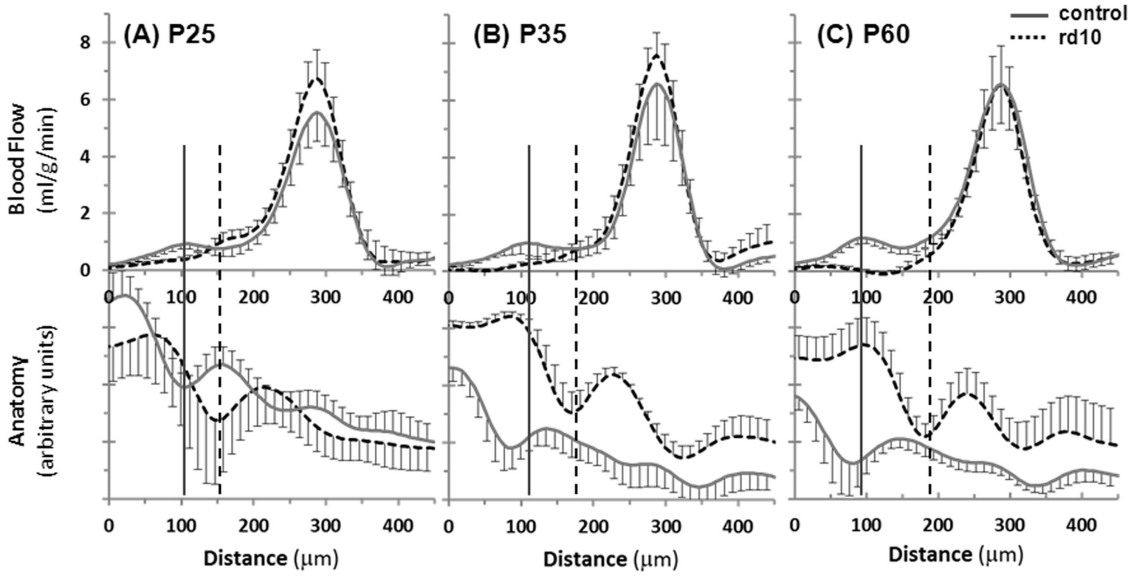

Figure 5.

Group average BF (top) and anatomical (bottom) profiles from control and rd10 mice at (A) P25, (B) P35, and (C) P60 (n=6 control and 6 rd10 at each age). The anatomical profiles come from the EPI images that the BF profiles were calculated from (and *not* from the bSSFP images) and were not intensity normalized. Error bars represent SD. The solid vertical lines indicate the approximate location of rBF in controls, and the dashed vertical lines indicate rBF in rd10 mice.

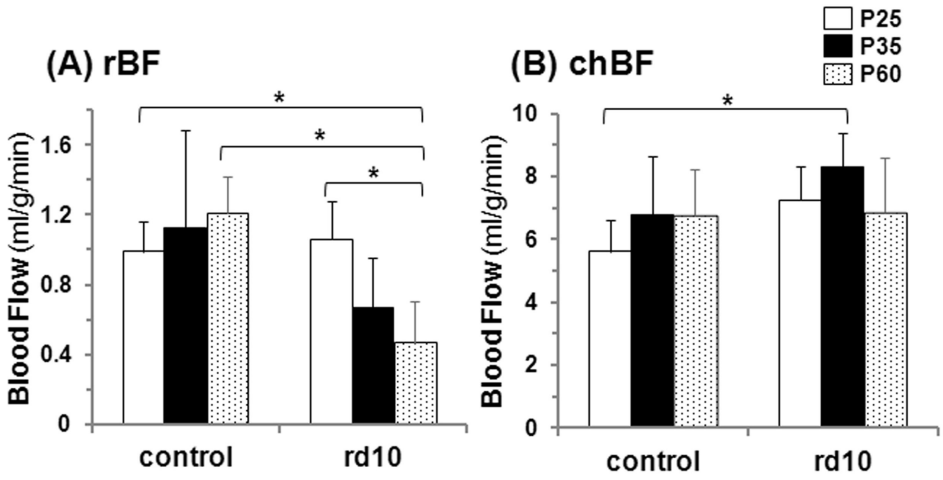

Figure 6.
Group average (A) retinal and (B) choroidal BF in control and rd10 mice at P25, P35, and P60. Error bars represent SD. *p<0.05.

Table 1

Physiological parameters during BF imaging from control and rd10 mice (mean±SD).

Age (days)	Strain	n	Weight (g)	Respiration Rate (breaths/min)	Heart Rate (beats/min)	O_2 Saturation (%)
25	control	6	14 ± 1	112 ± 7	483 ± 54	98.5 ± 0.6
	rd10	6	12 ± 1*	121 ± 10	421 ± 46	98.2 ± 1.1
35	control	6	18 ± 1	117 ± 6	475 ± 69	98.3 ± 0.3
	rd10	6	19 ± 1	118 ± 10	430 ± 35	98.7 ± 0.4
60	control	6	20 ± 2	117 ± 4	483 ± 41	98.6 ± 0.4
	rd10	6	18 ± 2	121 ± 7	524 ± 30	98.5 ± 0.1

* $p<0.05$ compared to age-matched control mice

Table 2

Thicknesses of histological layers from control and rd10 mice (μm, mean ± SD). Neural Retina is the sum of all layers. GCL – ganglion cell layer, IPL – inner plexiform layer, INL – inner nuclear layer, OPL – outer plexiform layer, ONL – outer nuclear layer, IS – inner segment, OS – outer segments. Please see Figure 3 for statistical tests.

Age (days)	Strain	n	GCL	IPL	INL	OPL	ONL	IS	OS	Neural Retina
25	control	6	24 ± 3	60 ± 9	40 ± 5	17 ± 2	58 ± 5	19 ± 1	22 ± 2	241 ± 19
	rd10	5	20 ± 1	54 ± 5	41 ± 2	12 ± 1	15 ± 3	8 ± 1		149 ± 5
35	control	5	18 ± 3	56 ± 4	39 ± 3	16 ± 1	58 ± 2	21 ± 1	22 ± 1	230 ± 12
	rd10	4	16 ± 3	53 ± 4	35 ± 3	8 ± 1	10 ± 3	3 ± 2		126 ± 2
60	control	6	22 ± 2	54 ± 3	41 ± 3	15 ± 1	56 ± 3	17 ± 2	26 ± 2	231 ± 8
	rd10	6	16 ± 3	40 ± 3	32 ± 2	9.7 ± 2		-	-	98 ± 7